Materials Science in Semiconductor Processing 202 (2026) 110125

Contents lists available at ScienceDirect

Materials Science in Semiconductor Processing

journal homepage: www.elsevier.com/locate/mssp

Capacitive-coupled non-pinched I–V and type II memristive behavior of carbon-TiO_2 nanocomposite films fabricated through aerosol flame synthesis

Abdul Khalique [a], Gianluigi De Falco [b,*], Patrizia Minutolo [b], Mario Commodo [b], Andrea D'Anna [a]

[a] Dipartimento di Ingegneria Chimica, dei Materiali e della Produzione Industriale, Università degli Studi di Napoli Federico II, Napoli, Italy
[b] Istituto di Scienze e Tecnologie per l'Energia e la Mobilità Sostenibili, Consiglio Nazionale delle Ricerche, Napoli, Italy

ARTICLE INFO

Keywords:
Aerosol flame synthesis
Carbon-TiO_2 nanomaterials
Nanostructured films
Non-pinched hysteresis
Capacitive-coupled memristive

ABSTRACT

Titanium dioxide (TiO_2) is a long-established semiconductor material used in several electrical and electronical applications, including random-access memories, biohybrid interfaces, sensors, and neuromorphic computing. Nevertheless, such applications are still at an early development stage, constrained by fundamental gaps in understanding and technological limitations. Functional memristive characteristics of TiO_2 rely extensively on the processes, including synthesis techniques, fabrication, and physicochemical modifications. In this work, nanostructured composite films of Carbon (Soot) and TiO_2 are fabricated through a custom-made aerosol flame synthesis (AFS) reactor using a facile one-step synthesis technique with good control over nanostructure, crystallinity, defect chemistry and carbon component inclusions. Scanning mobility particle sizer (SMPS) was employed to analyze particle size distribution in the flame. Microstructures and composition of the C-TiO_2 film were characterized through Raman spectroscopy, UV–VIS spectrophotometry, atomic force microscopy (AFM), and current-voltage I-V measurements. The presence of carbon and TiO_2 across the film was confirmed by the Raman spectrum and quantified by light absorption. The electrical characterization demonstrated a capacitive-coupled non-zero crossing and type-II hysteresis behavior of the C-TiO_2 nanostructured film. Following carbon compositing, TiO_2 exhibited enhanced optical absorption in the visible spectral region and electrical conductivity. The improvement in the conduction pathways was evidenced by the I-V measurements of the TiO_2 film and the C-TiO_2 film. A phenomenon of disappearance and reappearance of the capacitive-coupled memresistive effect was observed after dark and sunlight exposure, most likely due to the photosensitive nature of TiO_2 in the nanocomposite film. This proof-of-concept study testifies that, due to such properties, C-TiO_2 nanocomposite films produced via AFS can be considered as promising future candidates for applications in the field of next-generation electronic devices.

1. Introduction

Aerosol flame synthesis (AFS) is a widely used technique for the cost-effective production of novel functional nanomaterials [1–3]. Its versatility and capability for scaling up to industrial-level production make it an attractive choice. AFS is particularly proficient in controlling key features such as phase purity, crystallinity, and particle size, making it suitable to produce nanomaterials intended for advanced applications [4].

In the AFS process, particles are formed from gaseous pyrolysis products using a continuous flow method that involves introducing precursors into the flame. In addition to producing nanopowders, the AFS technique offers significant potential for fabricating nanostructured films and self-assembled coatings through thermophoretic deposition [1–5].

Among various compounds, titanium dioxide (TiO_2) is the second most synthesized material produced through flame reactor synthesis [2,6]. TiO_2 is a semiconductor material extensively researched for various advanced applications due to its chemical stability, photoactivity, and abundance. These applications include photovoltaics [7],

* Corresponding author. Istituto di Scienze e Tecnologie per l'Energia e la Mobilità Sostenibili (STEMS) - CNR, P.le V. Tecchio 80, 80125, Napoli, Italy.
E-mail address: gianluigi.defalco@stems.cnr.it (G. De Falco).

https://doi.org/10.1016/j.mssp.2025.110125
Received 18 June 2025; Received in revised form 8 September 2025; Accepted 4 October 2025
Available online 9 October 2025

electrochemical cells [8], photocatalysis [9], water treatment [10,11], anti-corrosive and antibacterial coatings [12,13], biomedical uses [14], sensors [15], and memory devices [16,17]. Comprehensive studies on TiO_2 production primarily focus on its anatase and rutile phases [18–21].

Practical applications of TiO_2 are often limited due to its wide bandgap, low absorption capacity, high electron-hole recombination rate, and relatively low activity under visible light [22,23]. TiO_2 has been studied extensively with metal and non-metal dopants to enhance its performance and characteristics, such as to reduce the bandgap and undesirable recombination rate of photogenerated hole and electron pair for various applications [24]. Several studies have been reported to address these shortcomings via the introduction of nanocarbons in different forms, including graphene-TiO_2 composites, carbon-doped TiO_2 nanoparticles, and CNT-fullerene-TiO_2 composites [25–29]. Carbonaceous materials increase the visible light absorption of the composite, enabling it to perform under a wide spectrum of light that ultimately influences the chemical bonding (Ti-O-C bonds) formed between the carbon and titanium dioxide (TiO_2) [30,31]. Additionally, carbon is a highly stable, low-cost, and eco-friendly material that aids the conduction of electrons from electron-hole pairs to enhance the charge separation capacity of the titanium dioxide (TiO_2) [32,33]. Recently, there has been an increased interest in compositing TiO_2 with different forms of carbon produced via flame reactors [24]. Such a combination offers exceptional electrical properties because of carbon-metal oxide interactions. The C-TiO_2 nanocomposite can be potentially employed for several applications such as water splitting [34], degradation of pollutants [35], drug delivery [36], photovoltaics [37], energy storage devices [38], gas sensors [39], biosensors [40], flexible and wearable devices [41], light-emitting diodes [42], electrochemical fuel cells [43] and many more. A relevant potential application of interest lies in the resistive switching phenomenon observed in a composite nanostructured film produced by the integration of conductive carbon material and semiconductor TiO_2 [44,45].

For these reasons, C-TiO_2 nanocomposite can be a promising candidate for applications in next-generation electronic devices because of the ideal C-TiO_2 combination where resistive switching characteristics of TiO_2 semiconductor material are aided by excellent optoelectrical properties and highly stable mechanical properties of the carbon compound [46,47].

In this work, we present the structure and properties of a nanostructured film of C-TiO_2 nanoparticles produced by a customized AFS reactor through a one-step process. The nanocomposite film is fabricated through thermophoretic deposition of C-TiO_2 nanoparticles on the substrate mounted on a rotating disk above the flame reactor. The prepared nanostructured C-TiO_2 film is investigated in-depth through various characterization techniques for different characteristics, including morphology, particle size distribution, chemical composition, optical properties, and electrical properties. The primary aim of this proof-of-concept study is to establish the feasibility of AFS in synthesizing in a single step functional nanostructured composite films of carbon and titania with specific optical and electrical properties for possible applications in novel electronic devices.

2. Experimental

The nanostructured C-TiO_2 particles were synthesized using a custom-designed aerosol flame reactor tailored for precise control of reaction parameters. It consists of a honeycomb burner and a high-pressure syringe pump used for loading precursor solution as a spray

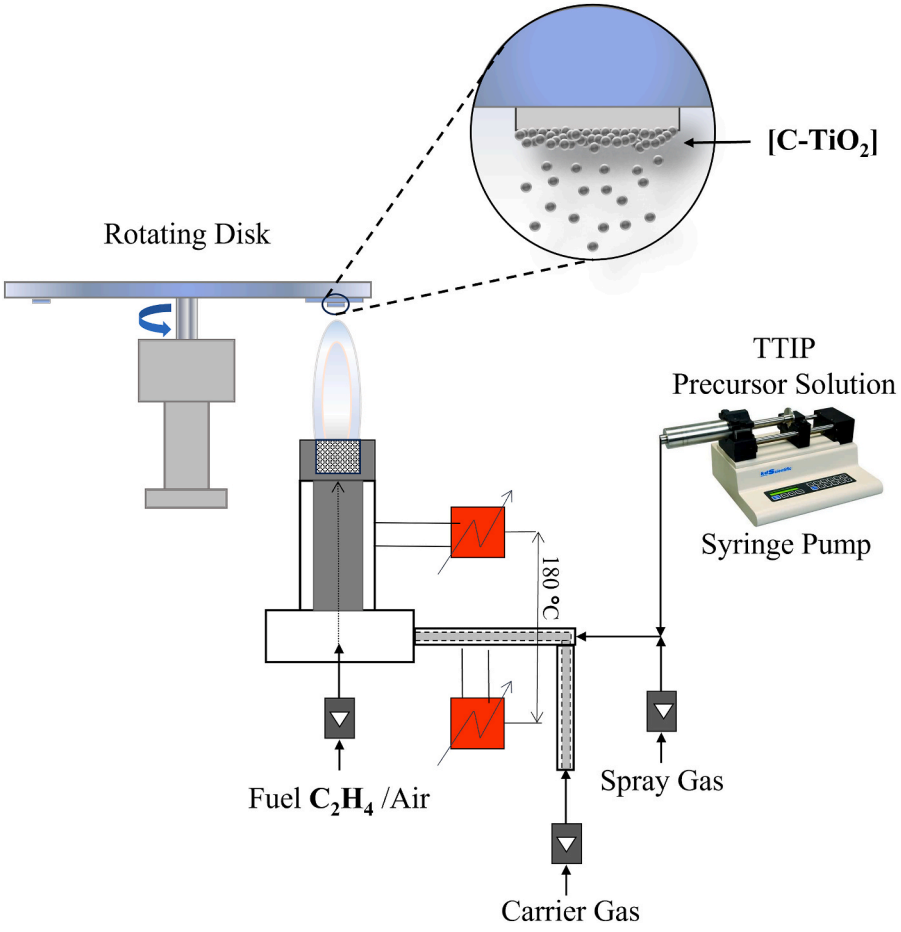

Fig. 1. Schematic of the experimental set-up for the synthesis and deposition of C-TiO_2 nanoparticles.

with the help of supplementary spray air and a pre-heated air flow as a carrier gas [5,48]. A schematic of the experimental set-up for the synthesis and deposition of C-TiO_2 particles into nanostructured films is reported in Fig. 1.

Titanium (IV) isopropoxide (TTIP) serves as the precursor for synthesizing TiO_2, whereas carbon material is obtained by running the flame in fuel-rich conditions. A 0.5 M TTIP solution was prepared in ethanol, sonicated for 1 h to ensure homogeneity, and then infused into the flame reactor at a controlled rate of 900 μL/min. Two additional flame conditions have been investigated: a fuel-rich flame without TTIP (the TiO_2 precursor), namely a Sooting flame, and a fuel-lean flame producing only TiO_2 nanoparticles, namely a TiO_2 producing flame.

The C/O ratio, equivalence ratio (Φ), cold gas velocity, and other relevant parameters for all three flame configurations, i.e., the C-TiO_2 producing flame, the Soot producing flame, and the TiO_2 producing flame, are summarized in Table 1.

The C/O ratios and the related equivalent ratios are calculated according to the combustion reaction of the fuel mixture composed of ethylene and ethanol with air. The change in C/O produced by the addition of TTIP in both the TiO_2 and C-TiO_2 flames is negligible. Indeed, by taking into account the contribution of TTIP to the total flow rates of fed gases, the variations of the cold gas velocity and the C/O ratio in the flame reactors are in the order of 1 %.

The C-TiO_2 and Soot flame reactors were operated under fuel-rich, soot-forming conditions to generate carbon precursors for nanomaterial synthesis. The only difference between the two flames was the presence of a titanium precursor in the C-TiO_2 reactor. In contrast, the TiO_2 flame reactor was operated under fuel-rich but non-sooting conditions to produce pure TiO_2 nanoparticles.

Temperatures were measured at a fixed location (15 mm) in the flames using a fast insertion procedure with a R-type thermocouple (Pt/13 %Rh–Pt) and corrected for radiation losses [49].

Size distributions of the particles generated in the flame are measured online by a TSI 3938 Scanning Mobility Particle Sizer (SMPS) at 15 mm above the burner; particles were withdrawn from the flame through a horizontal dilution probe having an orifice of 0.3 mm.

The nanoparticles produced in the flame were also deposited via thermophoresis on different substrates for diverse characterizations. Substrates are mounted on a rotating disk positioned at a fixed height above the burner (HAB) with a total deposition time of $t_d = 30$ s. This serves as a stagnation surface for the flame reactor and enables the substrates connected to the disk to be quickly put into the flame repeatedly, as shown in Fig. 1.

Particles deposited on quartz substrates were analyzed by Raman spectroscopy to evaluate their chemical composition. Quartz substrates were also used for UV–vis light absorption measurements and optical band gap analysis.

Raman spectroscopy analysis was carried out using Horiba XploRA microscope equipped with an objective lens of 100X and a Nd:YAG laser with an excitation wavelength of $\lambda = 532$ nm. An Agilent UV–Vis 8453 spectrophotometer was used to measure ultraviolet and visible light absorption spectra.

Muscovite mica substrates are used for the surface topography of the produced films through atomic force microscopy (AFM). Supersharp silicon probes (SSS-NCHR) were mounted on a scanning probe microscope by NT-MDT (NTEGRA) that performed the surface topography in semi-contact mode in ambient environmental conditions.

Micrux ED-IDE1-Au electrodes are used for the electrical characterization of the deposited particle film. Electrical measurements were carried out through a source measurement unit (SMU, Ossila B.V., NL) coupled with an electrode-holding chamber (Linkam Scientific Instruments Ltd., UK). This measurement unit, operated by computer-connected software, has a measurement range of −10 V to +10 V with variable voltage increment (VI) and voltage scan rate (VSR) functions set at VI = 0.5 V and VSR = 5.3 V/min.

Table 1
Investigated flame reactor parameters.

	C-TiO_2 Flame	Soot Flame	TiO_2 Flame
C/O ratio	0.87	0.87	0.58
Equivalence ratio Φ	2.78	2.78	1.98
Cold gas velocity (cm/s)	42.5	42.5	52
Liquid EtOH solution (μL/min)	900	900	900
TTIP concentration (M)	0.5	0	0.5

3. Results & discussion

A preliminary investigation was conducted at various heights above the burner (HAB) in the three flame configurations, to find the optimal conditions for the C-TiO_2 composite formation. To this aim, particles were sampled on quartz substrates and analyzed by light absorption and Raman spectroscopy. Soot formation was observed to initiate at lower HABs than TiO_2 particles' inception height. Among the tested configurations, the optimal conditions for achieving a well-integrated C-TiO_2 composite were identified at a HAB of 15 cm, where a favorable balance between soot formation and titanium dioxide nanoparticle growth was established. This is evident from Fig. 2 where the Raman spectra measured in C-TiO_2 flame at the two HAB of 10 cm and 15 cm are reported.

At HAB = 10 cm, the spectra exhibit only the characteristic D (~1350 cm^{-1}) and G (~1600 cm^{-1}) bands, which correspond to the A_{1g} breathing mode of aromatic rings in disordered carbon and the E_{2g} stretching mode of graphitic carbon, respectively. Notably, no Raman-active modes associated with the anatase polymorph of TiO_2 are observed, particularly the prominent $E_{g(1)}$ mode typically appearing around 144 cm^{-1}. This absence suggests that under the thermal and chemical environment present in the flame up to the height of 10 cm, TiO_2 fails to nucleate or remains in a non-crystalline, possibly amorphous state [50,51]. In contrast, at HAB = 15 cm, the Raman spectra reveal distinct features of crystalline anatase TiO_2: $E_{g(1)}$ (~146 cm^{-1}), B_{1g} (~393 cm^{-1}), A_{1g}/B_{1g} (~517 cm^{-1}), and $E_{g(2)}$ (~638 cm^{-1}) alongside the D and G bands of carbon. This suggests the successful formation of composite material. The crystallinity of TiO_2 at this HAB may be attributed to the higher flame residence time and favorable temperature gradients, which facilitate sufficient energy for anatase phase nucleation and growth [52,53].

Flame temperature was measured at a height above the burner (HAB) of 15 cm, which corresponds to the region chosen for nanoparticle deposition. The recorded temperatures were 1750 ± 50 K for both the pure carbon and C-TiO_2 flames, and 1720 ± 50 K for the TiO_2 flame. These values are quite similar, indicating that the thermal environments in both the C-TiO_2 and TiO_2 flames are comparable at this specific height, suggesting that they are not significant enough to affect nanoparticle formation.

Fig. 3(a) reports the Raman spectra of the three films produced collecting particles in the three different flames. TiO_2 can be produced either in the form of anatase or rutile, depending on the flame operating conditions [54]. The Raman spectrum of C-TiO_2 in Fig. 3(a) clearly shows the four characteristic peaks of titania attributed to the anatase phase along with the distinctive D and G bands of carbon.

The Raman spectrum corresponding to soot particles is also reported in Fig. 3(a). Notably, the D band and G bands in C-TiO_2 exhibit a similar spectral correspondence to those observed in the Raman spectrum of the pure carbon material. This strong resemblance suggests that carbon within the C-TiO_2 film is formed in a comparable structural configuration to that found in soot. Such an observation supports the conclusion that the carbon present in the C-TiO_2 composite film retains similar bonding characteristics and structural attributes.

Fig. 3(b) compares the anatase phonon modes observed in the Raman spectra of the pure TiO_2 nanoparticle film and that of the C-TiO_2 nanocomposite film. The prominent Raman peaks in the spectrum of the

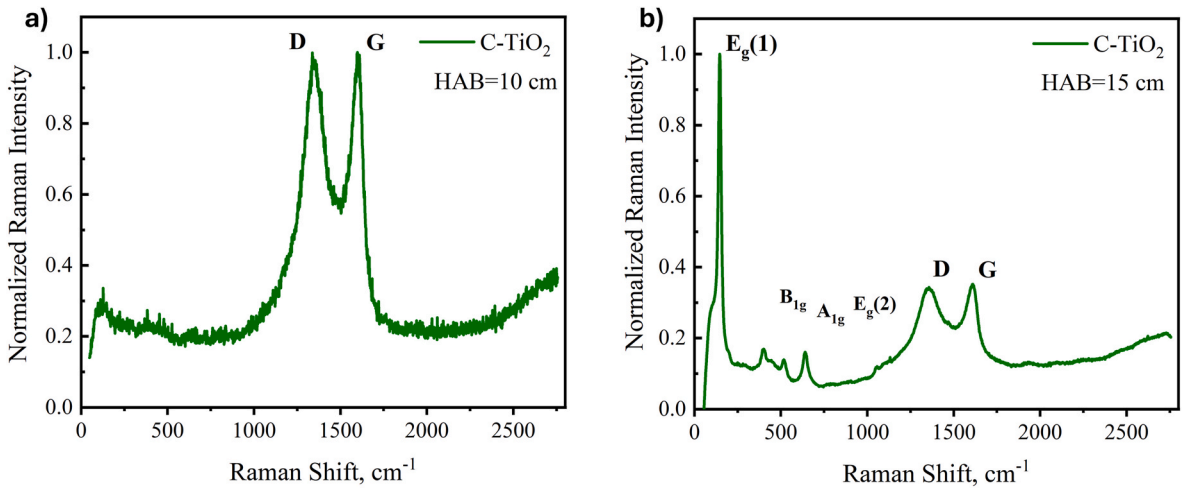

Fig. 2. Raman spectra of the film prepared in the C-TiO2 flame condition at HAB = 10 cm (a) and HAB = 15 cm (b).

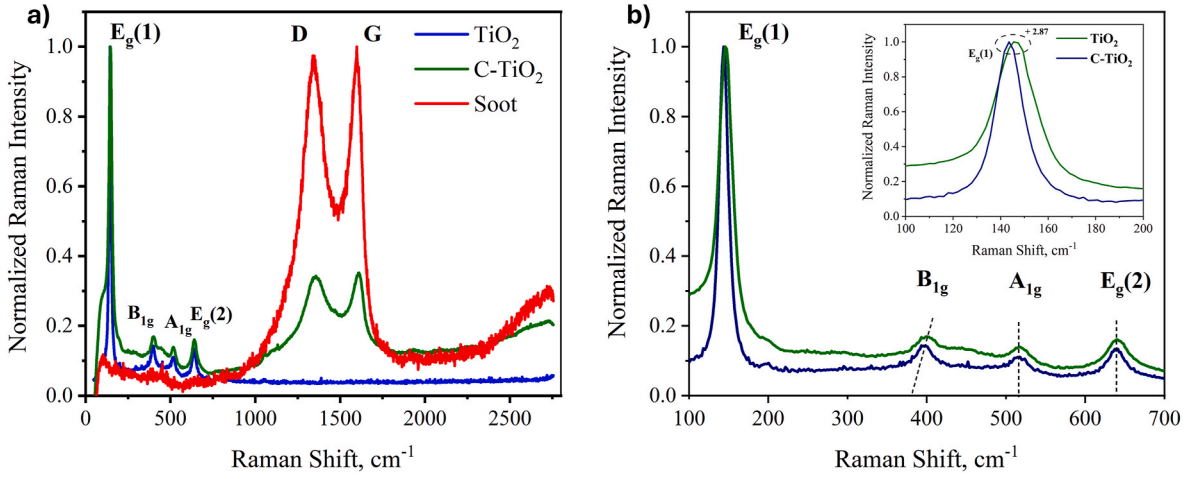

Fig. 3. Raman spectra of the C-TiO_2, TiO_2 and Carbon films (a) and signature peaks of the anatase mode of TiO_2 (b). The inset plot of Fig. 3(b) shows a magnification of the $E_g(1)$ peak.

pure TiO_2 film are positioned at 144 cm^{-1}, 393 cm^{-1}, 517 cm^{-1}, and 638 cm^{-1}. In contrast, the C-TiO_2 nanocomposite spectrum shows a blue shift of 2.87 cm^{-1} in the main anatase $E_{g(1)}$ peak, appearing at 146.87 cm^{-1}, as highlighted in the magnification of $E_{g(1)}$ peak reported as inset plot in Fig. 3(b). Additionally, a slight shift in the B_{1g} phonon mode of anatase is also observed. This shift indicates interactions between TiO_2 and other elements - specifically carbon [50]. These blue shifts are likely due to the high concentration of oxygen vacancies in the TiO_2, which interact with the carbon nanoparticles in the nanocomposite film [51]. This spectral shift supports the strong connection between the carbon matrix and the TiO_2 matrix. The evidence of structurally integrated C-TiO_2 composite with synergistic properties is crucial for ensuring efficient electron-hole separation, photostability, and surface reactivity, which are critical for applications in photocatalysis, electrocatalysis, and energy storage devices [55,56].

Moreover, the nanoscale interface formed between the conductive carbon material and semiconducting titanium dioxide is promising in a bid to investigate the possible resistive switching behavior of the composite nanomaterial. The switching behavior of a material is primarily attributed to the formation and migration of oxygen vacancies within the TiO_2 lattice, as well as the dynamic modulation of charge transport across the carbon–TiO_2 interface. These interfacial phenomena critically influence the ON/OFF resistance states, switching endurance, and data retention capabilities of the memory device, making the engineering of such nanocomposites a pivotal aspect of emerging non-volatile memory technology development [57]. Information on the carbon matrix can be derived by the analysis of the intensities of the D and G bands, I(D) and I (G), and the comparison between the spectra of the C-TiO_2 nanostructured film and the reference soot film. The D-band to G-band intensity ratio, I(D)/I(G) ratio, is close to 1 in both cases. Specifically, the calculated I(D)/I(G) ratio for C-TiO_2 is 0.95, while for soot nanoparticles, it is slightly higher, about 0.97. The marginal difference between these values indicates that the structural characteristics of the soot embedded in the C-TiO_2 film closely resemble those of standalone soot nanoparticles, C-TiO_2 matrix likely retains the disordered yet graphitic-like nature at nanoscale, typical of soot. This finding is significant as it provides insight into the structural properties of carbon within the C-TiO_2 system, which may influence its electronic, optical, and catalytic behaviors.

The size distribution of the particles (PSD) collected from the C-TiO_2 flame at HAB = 15 mm is reported in Fig. 4(b) and compared to the size distribution of the particles produced in the pure TiO_2 and soot flames in Fig. 4(a) and (c), respectively.

Fig. 4(a) shows that the particles measured for the pure TiO_2 have sizes primarily between 10 nm and 30 nm, with the tail of the particles decreasing by three orders of magnitude up to 60 nm. In Fig. 4(b), it is evident that the particle size of the nanocomposite C-TiO_2 is similar to that of the pure TiO_2 nanoparticles in the range up to 40 nm, with the

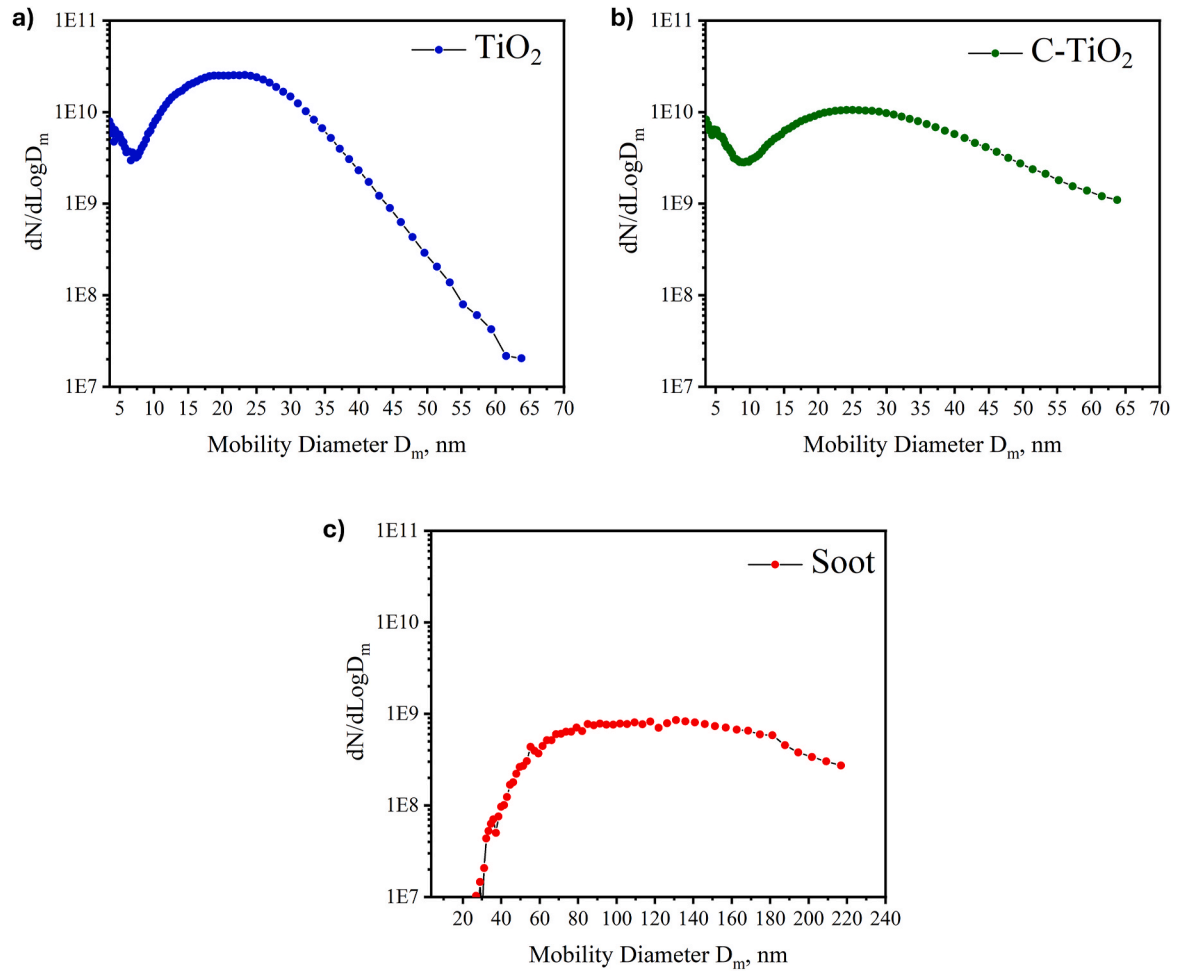

Fig. 4. Particle size distribution functions of TiO_2 nanoparticles (a), C-TiO_2 nanoparticles (b) and soot particles (c).

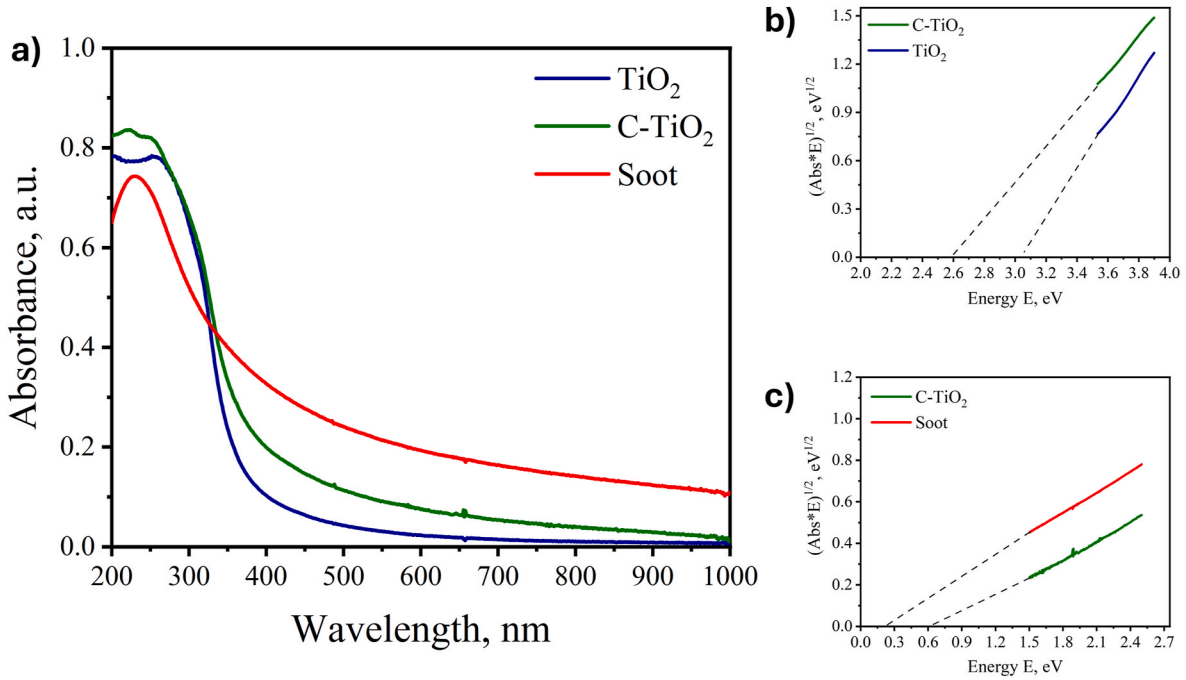

Fig. 5. UV–VIS Absorption spectra of TiO_2, C-TiO_2 and soot films (a). Optical bandgap of TiO_2 and C-TiO_2 films in the range 3.5–3.9 eV (b). Optical bandgap of TiO_2 and C-TiO_2 films in the range 1.5–2.5 eV (c).

presence of a first mode of particles smaller than 10 nm and a second mode centered at about 25 nm, although with a slightly lower number of the particles. The tail of this particle mode is much higher in the C-TiO_2 flame. This increase in the particle size can be ascribed to the compositing of the carbon with the TiO_2 nanoparticles. Indeed, Fig. 4 (c) shows that soot nanoparticles synthesized through the same flame reactor under identical conditions and at the same height above the burner as in the C-TiO_2 flame but without precursor infusions are larger than 40 nm, exhibit low number concentration, and have a broad size distribution with some particles exceeding 100 nm.

The significantly larger particle size of soot compared to TiO_2-based particles indicates a reduced particle growth when TiO_2 is present. It might be hypothesized that TiO_2 nanoparticles, experiencing strong electrostatic stabilization due to their metal oxide nature, reduce particle agglomeration. In flame synthesis, particularly within premixed stagnation flame setups, the formation of TiO_2 nanoparticles can significantly influence the agglomeration behavior of soot particles. The presence of TiO_2 nanoparticles has been observed to inhibit the growth of larger soot aggregates, leading to a reduction in overall particle size. This phenomenon is primarily attributed to the electrostatic stabilization conferred by TiO_2 nanoparticles [58].

Fig. 5 reports the UV–VIS absorption spectra of nanoparticle films. In Fig. 5(a), the spectrum for C-TiO_2 films is shown and compared to the absorption spectra of soot films and pure TiO_2 nanoparticle films. The absorption spectrum of pure titanium dioxide TiO_2 exhibits a pronounced absorption peak in the ultraviolet (UV) region, reflecting the typical behavior of this wide band bandgap semiconductor, whose strong UV absorption arises from electronic transitions between the valence and conduction bands [59]. Even though pure TiO_2 should theoretically only absorb in the UV region, the TiO_2 curve shows some absorption in the visible range which is indicative of defects such as oxygen vacancies, and other sources of disorder in the perfect crystal lattice that cause a gradual tailing off of absorption into lower energies the Urbach tail which can contribute to visible light absorption [60].

The spectrum of the carbon composited titanium dioxide C-TiO_2 presents the strong UV absorption band produced by the TiO_2 component, while the absorption in the visible range is sensibly stronger than the TiO_2 tail. Such extended absorption in the visible range above 450 nm show a strong similarity to the spectra of pure carbon and, therefore, can be due to the carbon addition, which also may result in creation of localized electronic states within the TiO_2 bandgap, hence further facilitating visible-light absorption [61]. The slightly stronger absorption in the UV range of the C-TiO_2 spectrum compared to the TiO_2's one, may also be attributed to the presence of carbon component which may also contribute to the modification in the material's electronic structure. In Fig. 5(b), the optical energy bandgap $E_{g,opt}$ of the pure TiO_2 and C-TiO_2 is reported. The optical bandgap $E_{g,opt}$ was calculated from the absorption spectra using Tauc analysis method [62,63]. $E_{g,opt}$ for TiO_2 spectrum and C-TiO_2 spectrum analyzed in the range of 3.5–3.9 eV provides $E_{g,opt}$ = 3.05 eV for the pure TiO_2 ascribed to the anatase polymorphic phase of TiO_2, whereas the $E_{g,opt}$ for the C-TiO_2 is 2.6 eV. Such TiO_2 optical bandgap reduction observed in C-TiO_2 spectrum can be attributed to the carbon compositing and can indicate a strong connection and effective compositing between carbon and TiO_2. In Fig. 5 (c), the optical band gap $E_{g,opt}$ of soot, determined within the range of 1.5 eV–2.5 eV, is presented for both the pure carbon film spectrum (depicted in red) and the C-TiO_2 composite film (in green). $E_{g,opt}$ for soot in the pure carbon film is 0.2 eV, whereas in the C-TiO_2 composite film, the optical band gap increases to 0.6 eV. This observed difference in the optical band gap of soot in the two spectra suggests a carbon-TiO_2 interaction which could alter the electronic states and modify the overall band structure.

From UV–Vis absorbance spectrum, the bulk layer thickness of nanoparticles composing the film, i.e., the thickness of the material in the absence of voids, can be derived using the well-known Lambert-Beer law and the refractive index of titania and soot. For anatase TiO_2 an extinction coefficient k = 0.48 at λ = 345 nm was used [64], while for soot an extinction coefficient k = 0.56 at λ = 532 nm was used [65]. The bulk thickness obtained from UV–Vis spectra were then used to calculate the mass loading of particle layers in each film, i.e., the actual mass of particles in the film per unit area, assuming a density of anatase nanoparticles equal to 4 g/cm^3 and a density of soot nanoparticles equal to 1.8 g/cm^3. In the pure carbon flame, the mass loading of soot was determined to be 6.9×10^{-6} g/cm^2, while in the pure titanium dioxide flame, the mass loading of TiO_2 was measured at 2.7×10^{-5} g/cm^2. When considering the composite C-TiO_2 film, the mass loading of soot was found to be 2.8×10^{-6} g/cm^2, and the mass loading of TiO_2 in the same film was 2.7×10^{-5} g/cm^2. From these measurements, the carbon-to-TiO_2 mass ratio in the C-TiO_2 composite film was calculated to be 0.1. This suggests that, in the composite film, the soot content is significantly lower than the TiO_2 content, indicating a predominance of titanium dioxide in the film structure.

Fig. 6 shows the atomic force microscopy (AFM) images of the produced nanostructured C-TiO_2 film. The surface morphology, homogeneity, and particle dispersion were carefully evaluated through obtaining high-resolution topographical images, enabling the evaluation of the homogeneity and the distribution of the nanoparticles inside the film. The AFM images in Fig. 6(a), acquired over an area of 20 × 20 μm^2, and in Fig. 6(b), acquired over an area of 10 × 10 μm^2, show uniformly dispersed nanostructures across the film. Furthermore, the 5 × 5 μm^2 and 1.5 × 1.5 μm^2 zoomed images of the C-TiO_2 nanocomposite film, reported respectively in Fig. 6(c) and (d), show that the film has a fractal-like structure. The particle uniformity in shape and size inside these evenly dispersed microclusters indicates a steady and regulated synthesis process, and it helps to ensure stability and homogeneity throughout the surface, as this structural arrangement is a necessary assurance for functional characteristics of the film for intended uses [66].

Fig. 7 reports the current voltage (I-V) measurements of the prepared samples on the synthesis day. The I-V curves measured on C-TiO_2 film are characterized by a hysteresis loop in the first and in the third quadrants, which is clearly symmetrical, non-pinched (i.e., non-origin or non-zero crossing) and it doesn't have any self-crossing point.

An ideal memresistive material is typically characterized by a resistive switching effect and usually shows fingerprint properties such as limiting linear I–V properties, single-valued charge-flux relation and particularly a pinched hysteresis current-voltage loop [67–69]. However, many works report the electrical characterization of materials that are unable to show all fingerprint properties and therefore they are defined as non-ideal memristive material [70]. One of the most common non-ideal behaviors is the non-zero I–V crossing behavior [68]. The non-zero I–V crossing property is typically due to the dominance of either mem-capacitive or mem-inductive memory effect, and two types of hysteresis loops can be identified as type-I (self-crossing or transversal) and type-II (not self-crossing or tangential) [71]. The AFS-made nanocomposite C-TiO_2 film exhibits an interesting electrical behavior as shown in Fig. 7 (a). Unlike the usual ribbon-like memristive hysteresis of TiO_2 [72], the nanocomposite C-TiO_2 film shows a memristor as well as a capacitor effect. Indeed, the particular hysteresis pattern, showing a non-pinched (or non-zero) crossing and not self-crossing I-V hysteresis, is typical of capacitive-coupled non-zero hysteresis and type-II memristive effect [67,73] and it is due to the simultaneous presence of the capacitive effect.

From the electrical circuit perspective, a capacitive coupled memristive devices can be modeled as a parallel connection between an ideal memristor and a capacitor [73]. In these devices, there are usually many positive and negative ions in the active layer of a device. When an external electric field is applied, positive ions move in the direction of the external electric field and negative ions migrate toward the opposite direction. This motion results in accumulated ions at the interfaces between the electrodes and the active layer, and a capacitive effect is subsequently established [73]The memristive effect is explained as a

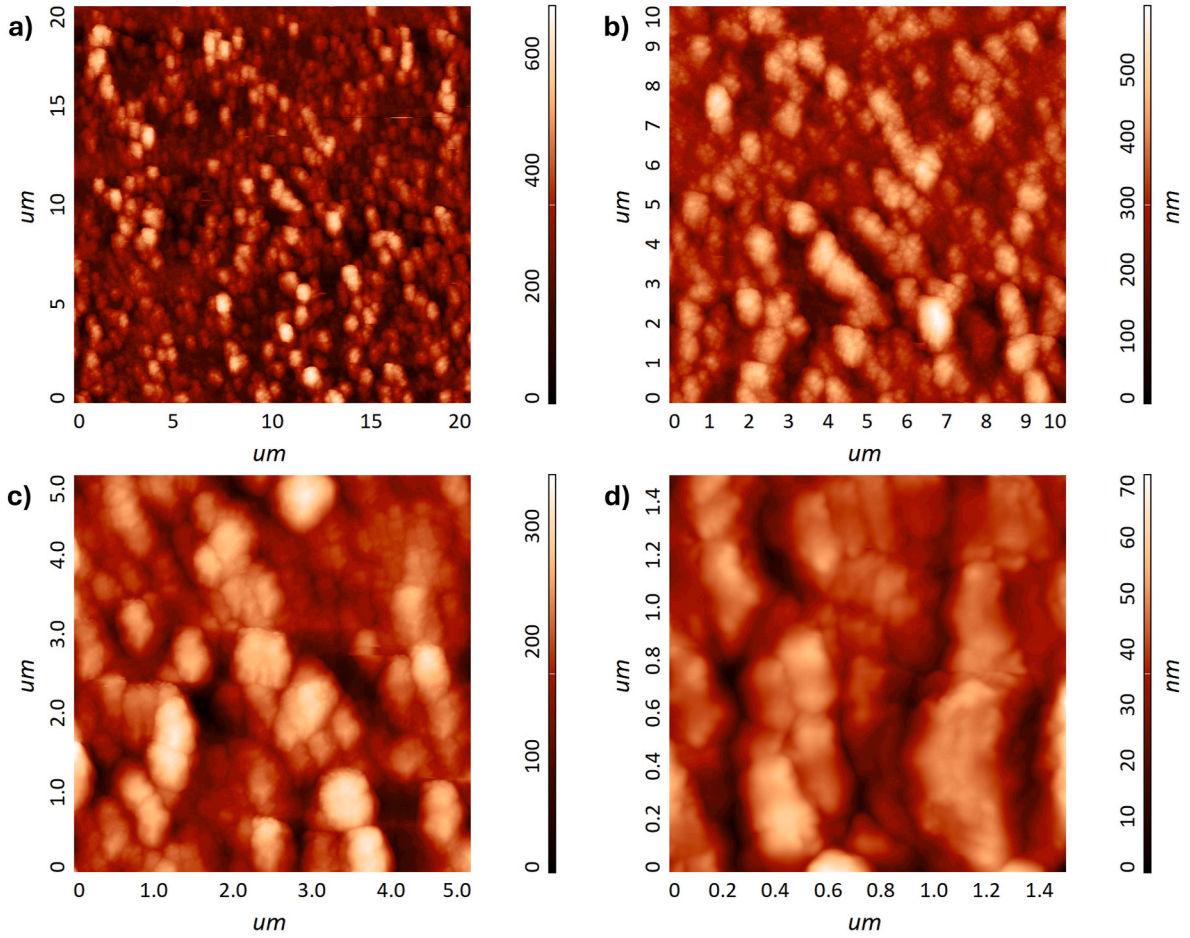

Fig. 6. AFM micrographs of the C-TiO_2 films over an area of 20 × 20 μm^2 (a), 10 × 10 μm^2 (b), 5 × 5 μm^2 (c) and 1.5 × 1.5 μm^2 (d).

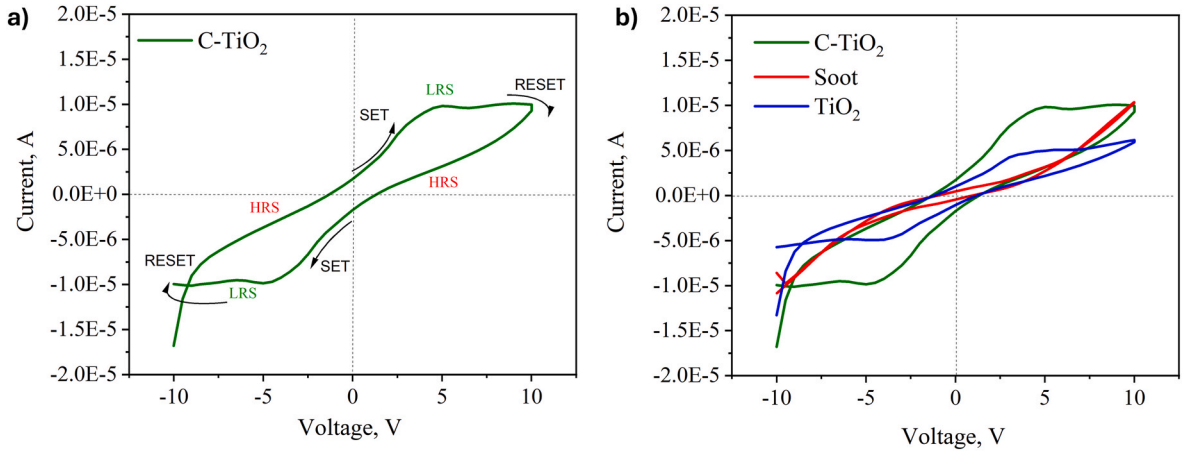

Fig. 7. Current voltage I-V curve measured on the synthesis day on C-TiO_2 film (a) and comparison between I-V curves measured on TiO_2 film, C-TiO_2 film and soot film (c).

resistive switching phenomenon where a material goes through reversible changes in the metastable resistance state induced by external applied electric fields [74]. Such changes are commonly referred to as occurring at the 'SET' and 'RESET' points of the memristive hysteresis, corresponding to the switching between the ON and OFF states, where a conductive filament is respectively formed and dissolved across the film. This filament is formed when the oxygen vacancies, which work as charge carriers, migrate toward the positive electrode and align upon reaching a certain voltage level under the application of an external electric field, thus favoring electrical conduction. Hence, a 'SET' process is responsible for the formation of the conductive filament, and the 'RESET' process is responsible for the rupture of that conducting filament. Fig. 7(a) shows a sharp transition in the curve starting from a high resistance state (HRS) to a low resistance state (LRS) at approximately +2V/-2V, indicating the material enters the 'SET' state. As the voltage continues to increase to its maximum, the material returns to the HRS, demonstrating a 'RESET' process. At an applied bias of +5 V, the device demonstrated a stable SET process, with the ON/OFF current ratio

between the low-resistance state (LRS) and high-resistance state (HRS) calculated to be approximately 3. The capacitive-coupled memristive behavior of the produced nanocomposite C-TiO_2 film suggests the feasibility of AFS in synthesizing nanomaterials that can be possibly integrated into next-generation electronic devices.

Fig. 7(b) shows a comparative analysis of TiO_2, soot, and nanocomposite C-TiO_2 film I-V hysteresis. Herein, three I-V hysteresis are reported where blue represents pure TiO_2, red represents carbon, and green represents C-TiO_2 films. It can be seen that the TiO_2 and C-TiO_2 hysteresis exhibit similar behavior but different current values, as the maximum current value for TiO_2 curve is 6.15×10^{-6} A and the maximum current value for the C-TiO_2 curve is 9.96×10^{-6} A, whereas the carbon curve exhibits a typical non-ohmic conductive behavior [5, 48]. Interestingly, the maximum current value of 1.03×10^{-5} is close to the maximum current value of the C-TiO_2 curve. Such I-V behavior explains the benefits of compositing TiO_2 with carbon, as the TiO_2 exhibits the capacitive-coupled memrstive behavior, the carbon addition, due to its electrical conductance, complements the TiO_2 with enhanced conduction paths during filament formation upon application of the external electric field. These nanostructured C-TiO_2 composite films possess very peculiar and attractive properties due to the combination of the optical properties of semiconductor TiO_2 with chemical and mechanical stability and conductive characteristics of the carbon compound [75]. It is worth underlining that the concurrent resistive and capacitive switching effects can be responsible for the performance degradation of the device in long run, i.e., in terms of long-term endurance, but could also augment the interest of research and industrial communities by introducing novel functionalities and thus applications [76]. Indeed, this capacitive coupled memristive effect of the materials has attained significant scientific attention, with a primary focus on development and optimization on their applications in future electronic devices. For instance, Mao et al. have presented an earth-abundant wheat flour (WF) as main dielectric component exhibiting a stable capacitive-coupled memristive behavior, highlighting the potential of biomaterials for sustainable device design [77]. Within this frame of reference, the results obtained on our presented C-TiO_2 films further complement this growing field by exhibiting a highly stable and repeatable electrical response under varying environmental conditions, as further confirmed by the measurements reported in the following. The ability demonstrated in the presented C-TiO_2 film to reversibly switch between linear and capacitive-coupled memristive states, while maintaining good cycle-to-cycle repeatability, underlines its potential as a promising platform material for future electronic devices.

Another interesting phenomenon was observed in the C-TiO_2 nanocomposite film upon putting the film in the dark for 48 h and then exposing it to sunlight for 12 h. The results are reported in Fig. 8. The sample was firstly stored in a dark environment for 48 h before subsequent electrical characterization to examine the stability and persistence of the capacitive-coupled memristive behavior in the synthesized C-TiO_2 thin film. As illustrated in Fig. 8(a), the post-storage I-V measurements revealed a significant change in the electrical response compared to the initial observations. Specifically, the previously observed capacitive-coupled memristive behavior was absent, and the I-V curve transitioned to a predominantly linear or weakly nonlinear characteristic. This drastic alteration in electrical properties suggests a degradation of the switching mechanism. due to the photosensitive properties of the semiconductor TiO_2. This effect is likely attributed to the loss of active charge carriers or the passivation of oxygen vacancy-related conductive pathways. A plausible explanation for this phenomenon is the gradual reabsorption of oxygen from the surrounding environment, leading to the neutralization of oxygen vacancies that initially facilitated the resistive switching process [78]. The reduced availability of defect states effectively inhibits the formation and rupture of conductive filaments, eliminating the hysteresis observed in previous measurements. Furthermore, a quantitative analysis reveals that electrical conductivity decreases by roughly one order of magnitude after 48-h of storage in dark further confirming the critical role of fact that the oxygen present in the surrounding plays a crucial role in modulating the film's electrical characteristics.

To further investigate the influence of environmental factors on the electrical properties of the C-TiO_2 film, the sample was subjected to continuous solar irradiation for 12 h. Fig. 8(b) shows the I-V hysteresis of the C-TiO_2 nanocomposite film after the sunlight exposure. The post-irradiation I-V curve reveals a remarkable recovery of the capacitive-coupled memristive behavior, which had previously degraded due to prolonged dark storage. Notably, the electrical conductivity exhibited a significant enhancement, increasing by approximately one and a half orders of magnitude compared to the initial measurements taken on the synthesis day. Reaching the value of 6.52×10^{-4} A. To confirm the repeatability of this phenomenon, the samples were passed through repetitive cycles of dark and sunlight multiple times. This pronounced recovery in memcapacitor effect and conductivity can be attributed to the photoinduced electrons in the TiO_2 matrix. When exposed to solar radiation, photons, and particularly those in the UV range, possess sufficient energy to excite electrons from the valence band to the conduction band, thereby facilitating oxygen desorption from the film. This process produces photoinduced surface oxygen vacancies (PI-SOVs), which are crucial for the formation and modulation of conductive filaments responsible for resistive switching. The produced oxygen vacancies reactivate the formation of conductive filaments, reinstating the capacitive-coupled memristive behavior observed in the initial I-V characteristics. These findings suggest that solar irradiation serves as an effective toll for modulating and rejuvenating the electrical properties of C-TiO_2 films. The reversible nature of the switching effect highlights the

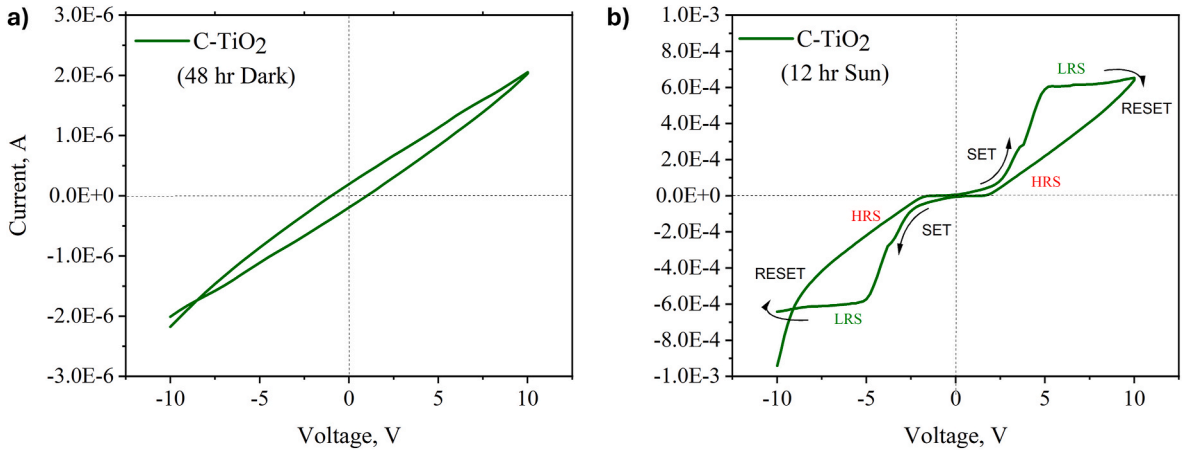

Fig. 8. Current-voltage I-V curves of C-TiO_2 film after 48 h in dark (a) and after 12 h exposure to the sunlight (b).

dynamic role of oxygen vacancies in governing the switching mechanism. Furthermore, this result underscores the potential of light-assisted recovery techniques for enhancing the long-term operational stability of TiO_2-based capacitive-coupled memristive devices.

The repeatability of such an I-V behavior was confirmed by performing 10 consecutive cycles of the electrical measurements on the same samples, as reported in Fig. 9.

Fig. 9(a) presents the repeatability of the C-TiO_2 I-V characteristics measured on the day of synthesis. The curves exhibit stable behavior over multiple consecutive cycles, confirming the robustness of the film response. Such outcome explicitly exhibits the capacitive-coupled memristive effect, with uniform current values and negligible cycle-to-cycle variation, highlighting the reproducibility of the phenomenon. Similarly, Fig. 9(b) and (c) illustrate the cyclic I-V stability of the C-TiO_2 film under different conditions. After 48 h in the dark, the device exhibits highly stable and linear cyclic behavior as shown in Fig. 9(b), with excellent repeatability across multiple cycles, indicating the disappearance of the capacitive-coupled memristive response. In contrast, after 12 h of solar exposure, the I-V curves in Fig. 9(c) once again display the capacitive-coupled memristive effect with consistent cycle-to-cycle performance and negligible current variation, confirming the robust repeatability of the film under varying environmental conditions. The repeatability of the I-V measurements throughout the several cycles under all tested conditions exhibit the intrinsic stability of the C-TiO_2 film. When measured on the synthesis day, the film demonstrates uniform capacitive coupled memristive effect with trivial cycle-to-cycle deviation, endorsing reproducible switching mechanism. While when tested after 48 h in dark, the film shows a linear ohmic-like behavior, exhibiting consistent cycle-to-cycle stability and highlighting disappearance of the capacitive coupled memristive effect. Remarkably, when tested after exposure to sunlight for 12 h, the film showed excellent recovery of capacitive coupled memristive effect with highly reproducible I-V curves that remain consistently stable across several cycles. Such observations endorse the reliability and robustness of the C-TiO_2 film, where repeatability directly indicates its long-term stability and potential suitability for practical electronic device applications.

The observed variations in I-V characteristics under different environmental conditions suggest that the capacitive-coupled memristive behavior of C-TiO_2-based devices can be effectively modeled and controlled through the regulation of oxygen vacancies within the film. The ability to modulate the electrical response by manipulating the availability and distribution of oxygen vacancies highlights their critical role in governing the resistive switching mechanism. This tunability presents an opportunity to develop strategies for optimizing device performance and reliability in practical applications and highlights the potential for light-assisted modulation of switching characteristics. The ability of UV photons to restore oxygen vacancies and enhance conductivity suggests a promising pathway for achieving multilevel resistive switching through controlled light exposure [79–81]. This phenomenon could be leveraged to develop opto-electronically tunable memory devices, where different resistive states can be programmed and stabilized using targeted light exposure. Such a capability would be highly advantageous for advanced non-volatile memory technologies and neuromorphic computing applications, where precise control over multiple resistance states is essential for enhancing storage density and computational functionality. Overall, these findings emphasize the

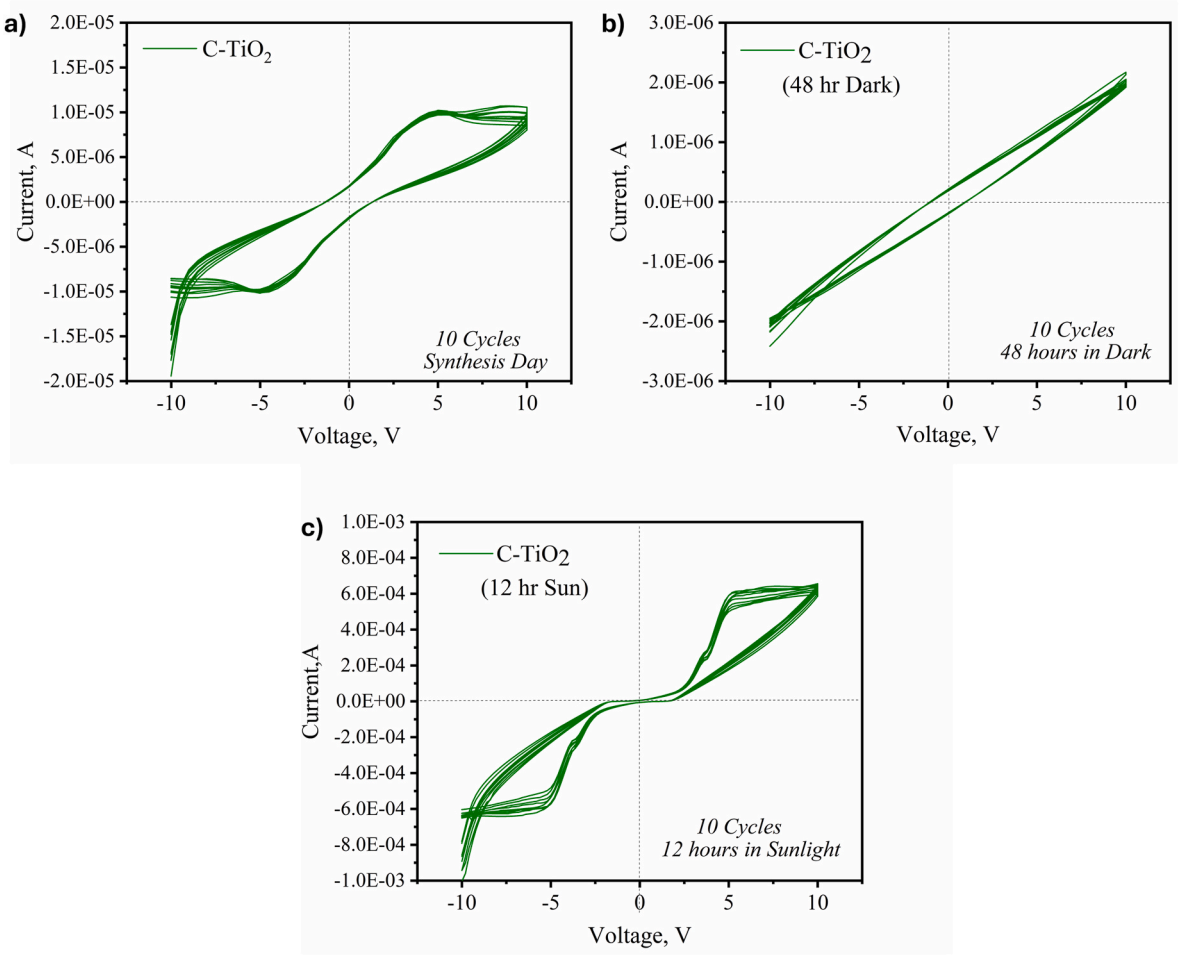

Fig. 9. I-V measurements on C-TiO_2 film over 10 consecutive cycles on the synthesis day (a), after 48 h in dark (b) and after 12 h exposure to the sunlight (c).

significance of oxygen vacancy engineering and light-assisted modulation in C-TiO_2-based capacitive-coupled memristive devices. Future research should be devoted to exploring in depth the quantitative relationship between light intensity, exposure duration, and the extent of capacitive-coupled resistive switching recovery in C-TiO_2 materials. Also, further work needs to be performed to understand how the effective resistance and capacitance of the nanocomposite material can be modulated simultaneously by appropriate voltage pulsing and/or by varying the ambient parameters such as humidity.

4. Conclusions

In this work, nanostructured C-TiO_2 composite films were produced via a one-step flame synthesis technique, through thermophoretic deposition of C-TiO_2 nanoparticles on different substrates placed on the rotating disk mounted at a height of 15 cm above the burner.

The interaction between carbon and TiO_2 was revealed by the Raman spectrum. All four peaks corresponding to the active anatase modes of TiO_2 were observed along with pronounced peaks of D band and G band centered at 1350 cm^{-1} and 1600 cm^{-1}, ascribed to the graphitic-like form of carbon. A blue shift in the high-intensity primary peak of anatase phase TiO_2 was observed suggesting successful compositing of carbon and TiO_2. Particle size distribution measured with a Scanning Mobility Particle Sizer showed a slight increase in the particle size of the C-TiO_2 as compared to the pure TiO_2 nanoparticles. UV–VIS spectrophotometry provided the absorption spectra for pure TiO_2, soot and nanostructured C-TiO_2 film. Optical energy bandgap $E_{g,opt}$ was calculated from the absorption spectra using Tauc plot method, which showed the significant reduction of 0.45 eV in the $E_{g,opt}$ of the TiO_2 component in the C-TiO_2 nanocomposite film with respect to that of the pure TiO_2 indicating strong interaction between carbon and TiO_2 in the produced film. AFM surface topography of the produced C-TiO_2 nanocomposite film showed that the film exhibited homogenous distribution of nanoparticles, with uniformity in size and shape.

The electrical characterization performed on the C-TiO_2 film revealed a capacitive coupled non-zero I–V and type-II memristive behavior. An enhanced electrical conductivity was measured in the C-TiO_2 nanocomposite film in comparison to the pure TiO_2 film. A phenomenon of disappearance and reappearance of the capacitive-coupled memresistive effect was observed after subsequent treatment C-TiO_2 film in the dark and sunlight for a period of 48 h and 12 h respectively. The observed phenomenon was most likely due to the photosensitive nature of the TiO_2 present in the C-TiO_2 nanocomposite film. This proof-of-concept study proves that AFS is an effective synthesis method to produce in a single step nanostructured films of C-TiO_2 nanoparticles with appealing characteristics due to the combination of the optical and electrical properties of semiconductor nano-TiO_2 with the chemical and mechanical stability and the conductive features of carbon nanomaterial.

CRediT authorship contribution statement

Abdul Khalique: Writing – original draft, Methodology, Investigation, Data curation, Conceptualization. **Gianluigi De Falco:** Writing – review & editing, Supervision, Methodology, Investigation, Conceptualization. **Patrizia Minutolo:** Writing – review & editing, Supervision, Conceptualization. **Mario Commodo:** Writing – review & editing, Supervision, Conceptualization. **Andrea D'Anna:** Writing – review & editing, Supervision, Conceptualization.

Declaration of competing interest

The authors declare that they have no known competing financial interests or personal relationships that could have appeared to influence the work reported in this paper.

Acknowledgments

The authors acknowledge financial support under the National Recovery and Resilience Plan (PNRR), Mission 4, Component 2, Investment 1.1, Call for tender No. 1409 published on 14.9.2022 by the Italian Ministry of University and Research (MUR), funded by the European Union – NextGenerationEU– Project Title: Integrating **FLA**me carbon/TiO2 nanostructured films into **ME**mbrane of electrospun **N**anofibers as **CO**atings for water treatment (**FLAMENCO**) – CUP E53D23017720001 - Grant Assignment Decree No. 1389 adopted on 01/09/2023 by the Italian Ministry of Ministry of University and Research (MUR).

Data availability

Data will be made available on request.

References

[1] M.Y. Manuputty, et al., Polymorphism of nanocrystalline TiO2 prepared in a stagnation flame: formation of the TiO2-II phase, Chem. Sci. 10 (5) (Jan. 2019) 1342–1350, https://doi.org/10.1039/C8SC02969E.
[2] K.B. Riad, P.M. Wood-Adams, K. Wegner, Flame-made TiO2(B), Mater. Res. Bull. 106 (Oct. 2018) 276–281, https://doi.org/10.1016/J.MATERRESBULL.2018.06.017.
[3] R. Strobel, S.E. Pratsinis, Flame aerosol synthesis of smart nanostructured materials, J. Mater. Chem. 17 (45) (Nov. 2007) 4743–4756, https://doi.org/10.1039/B711652G.
[4] B. Zhao, K. Uchikawa, J.R. McCormick, C.Y. Ni, J.G. Chen, H. Wang, Ultrafine anatase TiO2 nanoparticles produced in premixed ethylene stagnation flame at 1 atm, Proc. Combust. Inst. 30 (2) (Jan. 2005) 2569–2576, https://doi.org/10.1016/J.PROCI.2004.08.146.
[5] G. De Falco, L. Basta, M. Commodo, P. Minutolo, A. D'Anna, Flame synthesis of soot/TiO2 nanoparticle composite films with improved electrical properties characterized by Scanning Probe Microscopy, Proc. Combust. Inst. 40 (1–4) (Jan. 2024) 105475, https://doi.org/10.1016/J.PROCI.2024.105475.
[6] K. Wegner, S.E. Pratsinis, Scale-up of nanoparticle synthesis in diffusion flame reactors, Chem. Eng. Sci. 58 (20) (Oct. 2003) 4581–4589, https://doi.org/10.1016/J.CES.2003.07.010.
[7] A. Perrotta, C. Fuentes-Hernandez, T.M. Khan, B. Kippelen, M. Creatore, S. Graham, Near room-temperature direct encapsulation of organic photovoltaics by plasma-based deposition techniques, J. Phys. D Appl. Phys. 50 (2) (Jan. 2017), https://doi.org/10.1088/1361-6463/50/2/024003.
[8] S.Z. Khalajabadi, N. Ahmad, S. Izman, A. Bin Haji Abu, W. Haider, M.R. Abdul Kadir, In vitro biodegradation, electrochemical corrosion evaluations and mechanical properties of an Mg/HA/TiO2 nanocomposite for biomedical applications, J. Alloys Compd. 696 (Mar. 2017) 768–781, https://doi.org/10.1016/J.JALLCOM.2016.11.106.
[9] P.D. Tran, L.H. Wong, J. Barber, J.S.C. Loo, Recent advances in hybrid photocatalysts for solar fuel production, Energy Environ. Sci. 5 (3) (Mar. 2012) 5902–5918, https://doi.org/10.1039/C2EE02849B.
[10] M. Ali Memon, M. Wasim Akhtar, R. Shahbaz, N.M. Gabol, M. Yar Khuhawar, M. Yasir Khan, Biogenic synthesis of Ag-doped TiO2 photocatalyst using citrus paradisi extract for solar trigged degradation of methylene blue, Technology (Sindri) (2024), https://doi.org/10.3316/INFORMIT.T2024042500012090404456788.
[11] A. Shaikh, A. Khalique, M.W. Akhtar, M.A. Memon, Photoenhanced degradation of cationic dye (Methylene blue) using biogenic titania from Malus Domestica extract, ECS Trans. 107 (1) (Apr. 2022) 14313–14323, https://doi.org/10.1149/10701.14313ECST/META.
[12] G. De Falco, et al., Antimicrobial activity of flame-synthesized nano-TiO2 coatings, Environ. Sci. Nano 4 (5) (May 2017) 1095–1107, https://doi.org/10.1039/C7EN00030H.
[13] G. De Falco, et al., TIO2 nanoparticle coatings with advanced antibacterial and hydrophilic properties prepared by flame aerosol synthesis and thermophoretic deposition, Surf. Coat. Technol. 349 (Sep. 2018) 830–837, https://doi.org/10.1016/J.SURFCOAT.2018.06.083.
[14] Q. Junnan, L. Huimin, L. Guihong, C. Yao, Innovation of TiO2-x nanomaterials in the biomedical field: synthesis, properties, and application prospects, Chem. Eng. J. 491 (Jul. 2024) 151773, https://doi.org/10.1016/J.CEJ.2024.151773.
[15] J. Bai, B. Zhou, Titanium dioxide nanomaterials for sensor applications, Chem. Rev. 114 (19) (Oct. 2014) 10131–10176, https://doi.org/10.1021/CR400625J/ASSET/IMAGES/LARGE/CR-2013-00625J_0002.JPEG.
[16] A. Zaffora, F. Di Franco, R. Macaluso, M. Santamaria, TiO2 in memristors and resistive random access memory devices, in: Titanium Dioxide (Tio2) and Its Applications, Jan. 2021, pp. 507–526, https://doi.org/10.1016/B978-0-12-819960-2.00020-1.
[17] J. Pan, et al., Mimicking synaptic plasticity based on TiO2/MgO film resistive switching device, Mater. Sci. Semicond. Process. 197 (Oct. 2025) 109695, https://doi.org/10.1016/J.MSSP.2025.109695.

[18] A.K. Bhanwala, A. Kumar, D.P. Mishra, J. Kumar, Flame aerosol synthesis and characterization of pure and carbon coated titania nano powder, J. Aerosol Sci. 40 (8) (Aug. 2009) 720–730, https://doi.org/10.1016/J.JAEROSCI.2009.04.003.
[19] T. Dreier, C. Schulz, Laser-based diagnostics in the gas-phase synthesis of inorganic nanoparticles, Powder Technol. 287 (Jan. 2016) 226–238, https://doi.org/10.1016/J.POWTEC.2015.10.015.
[20] X. Liu, M.E. Smith, S.D. Tse, In situ Raman characterization of nanoparticle aerosols during flame synthesis, Appl. Phys. B 100 (3) (Sep. 2010) 643–653, https://doi.org/10.1007/S00340-010-4091-X/METRICS.
[21] S. Li, Y. Ren, P. Biswas, S.D. Tse, Flame aerosol synthesis of nanostructured materials and functional devices: processing, modeling, and diagnostics, Prog. Energy Combust. Sci. 55 (Jul. 2016) 1–59, https://doi.org/10.1016/J.PECS.2016.04.002.
[22] K. Hashimoto, H. Irie, A. Fujishima, TiO 2 photocatalysis: a historical overview and future prospects, Jpn. J. Appl. Phys., Part 1: Regular Papers and Short Notes and Review Papers 44 (12) (Dec. 2005) 8269–8285, https://doi.org/10.1143/JJAP.44.8269/XML.
[23] T. Van Gerven, G. Mul, J. Moulijn, A. Stankiewicz, A review of intensification of photocatalytic processes, Chem. Eng. Process. Process Intensif. 46 (9) (Sep. 2007) 781–789, https://doi.org/10.1016/J.CEP.2007.05.012.
[24] G. Kholodnaya, R. Sazonov, D. Ponomarev, TiO2@C nanocomposites – from synthesis to application: a review, Fullerenes, Nanotub. Carbon Nanostruct. 29 (7) (2021) 487–526, https://doi.org/10.1080/1536383X.2020.1820994.
[25] T. Tsumura, N. Kojitani, I. Izumi, N. Iwashita, M. Toyoda, M. Inagaki, Carbon coating of anatase-type TiO2 and photoactivity, J. Mater. Chem. 12 (5) (Apr. 2002) 1391–1396, https://doi.org/10.1039/B201942F.
[26] M. Toyoda, T. Yano, B. Tryba, S. Mozia, T. Tsumura, M. Inagaki, Preparation of carbon-coated Magneli phases TinO2n−1 and their photocatalytic activity under visible light, Appl. Catal., B 88 (1–2) (Apr. 2009) 160–164, https://doi.org/10.1016/J.APCATB.2008.09.009.
[27] Y.C. Hsu, H.C. Lin, C.W. Lue, Y.T. Liao, C.M. Yang, A novel synthesis of carbon-coated anatase nanocrystals showing high adsorption capacity and photocatalytic activity, Appl. Catal., B 89 (3–4) (Jul. 2009) 309–314, https://doi.org/10.1016/J.APCATB.2008.12.008.
[28] M. Chhowalla, H. Wang, N. Sano, K.B.K. Teo, S.B. Lee, G.A.J. Amaratunga, Carbon onions: carriers of the 217.5 nm Interstellar Absorption Feature, Phys. Rev. Lett. 90 (15) (Apr. 2003) 4, https://doi.org/10.1103/PHYSREVLETT.90.155504/FIGURES/5/MEDIUM.
[29] W.C. Oh, A.R. Jung, W.B. Ko, Characterization and relative photonic efficiencies of a new nanocarbon/TiO2 composite photocatalyst designed for organic dye decomposition and bactericidal activity, Mater. Sci. Eng. C 29 (4) (May 2009) 1338–1347, https://doi.org/10.1016/J.MSEC.2008.10.034.
[30] W. Fan, Q. Lai, Q. Zhang, Y. Wang, Nanocomposites of TiO2 and reduced graphene oxide as efficient photocatalysts for hydrogen evolution, J. Phys. Chem. C 115 (21) (Jun. 2011) 10694–10701, https://doi.org/10.1021/JP2008804/ASSET/IMAGES/LARGE/JP-2011-008804_0011.JPEG.
[31] Y. Zhang, Z.R. Tang, X. Fu, Y.J. Xu, TiO2-graphene nanocomposites for gas-phase photocatalytic degradation of volatile aromatic pollutant: is TiO2-graphene truly different from other TiO2-carbon composite materials? ACS Nano 4 (12) (Dec. 2010) 7303–7314, https://doi.org/10.1021/NN1024219/SUPPL_FILE/NN1024219_SI_001.PDF.
[32] H. Park, H. Il Kim, G.H. Moon, W. Choi, Photoinduced charge transfer processes in solar photocatalysis based on modified TiO2, Energy Environ. Sci. 9 (2) (Feb. 2016) 411–433, https://doi.org/10.1039/C5EE02575C.
[33] L. Zhang, M.S. Tse, O.K. Tan, Y.X. Wang, M. Han, Facile fabrication and characterization of multi-type carbon-doped TiO2 for visible light-activated photocatalytic mineralization of gaseous toluene, J Mater Chem A Mater 1 (14) (Mar. 2013) 4497–4507, https://doi.org/10.1039/C3TA01366A.
[34] S.K. Parayil, H.S. Kibombo, C.M. Wu, R. Peng, J. Baltrusaitis, R.T. Koodali, Enhanced photocatalytic water splitting activity of carbon-modified TiO2 composite materials synthesized by a green synthetic approach, Int. J. Hydrogen Energy 37 (10) (May 2012) 8257–8267, https://doi.org/10.1016/J.IJHYDENE.2012.02.067.
[35] H. Liu, K. Wang, D. Zhang, D. Zhao, J. Zhai, W. Cui, Adsorption and catalytic removal of methyl orange from water by PIL-GO/TiO2/Fe3O4 composites, Mater. Sci. Semicond. Process. 154 (Feb. 2023) 107215, https://doi.org/10.1016/J.MSSP.2022.107215.
[36] W. Guo, et al., Platelet membrane-coated C-TiO2 hollow nanospheres for combined sonodynamic and alkyl-radical cancer therapy, Nano Res. 16 (1) (Jan. 2023) 782–791, https://doi.org/10.1007/S12274-022-4646-2.
[37] Ç. Kırbıyık, et al., Enhancing the c-TiO2 based perovskite solar cell performance via modification by a serial of boronic acid derivative self-assembled monolayers, Appl. Surf. Sci. 423 (Nov. 2017) 521–527, https://doi.org/10.1016/J.APSUSC.2017.06.189.
[38] H. Wu, et al., Production of the C/TiO2 composite with a high-performance electrochemical property from titanium-rich sludge via in-situ C coating, J. Environ. Sci. 137 (Mar. 2024) 131–143, https://doi.org/10.1016/J.JES.2023.02.044.
[39] D. Zhao, et al., C-doped TiO2 nanoparticles to detect alcohols with different carbon chains and their sensing mechanism analysis, Sensor. Actuator. B Chem. 312 (Jun. 2020) 127942, https://doi.org/10.1016/J.SNB.2020.127942.
[40] M. Liu, G. Zhao, Y. Tang, H. Shi, N. Yang, Direct electrochemistry of hemoglobin on vertically aligned carbon hybrid TiO2 nanotubes and its highly sensitive biosensor performance, Chin. J. Chem. 31 (2) (Feb. 2013) 215–220, https://doi.org/10.1002/CJOC.201200883.
[41] H. Zheng, et al., TiO2@C core–shell nanowires for high-performance and flexible solid-state supercapacitors, J Mater Chem C Mater 1 (2) (Dec. 2012) 225–229, https://doi.org/10.1039/C2TC00047D.
[42] P.A. Ochoa Rodríguez, S.G. Casuscelli, V.R. Elías, G.A. Eimer, LED visible-light activated mesoporous TiO2: a better understanding about carbon role in the photocatalytic performance of solid, Catal. Today 372 (Jul. 2021) 198–210, https://doi.org/10.1016/J.CATTOD.2020.10.015.
[43] C.H. Sung, et al., Enhanced stability and electrochemical performance of carbon-coated Ti3+ self-doped TiO2-Reduced graphene oxide hollow nanostructure-supported Pt-Catalyzed fuel cell electrodes, Adv. Mater. Interfac. 4 (21) (Nov. 2017), https://doi.org/10.1002/ADMI.201700564.
[44] W. Jia, L. Hu, W. Gao, W. Mu, Z. Chou, X. Cheng, Improvement of switching uniformity in TiO2-based resistive random access memory with graphene oxide embedded film, Mater. Sci. Semicond. Process. 182 (Nov. 2024) 108688, https://doi.org/10.1016/J.MSSP.2024.108688.
[45] L. Hu, Z. Zheng, M. Xiao, Q. Meng, Enhanced resistive switching performance of TiO2 based RRAM device with graphene oxide inserting layer, Semicond. Sci. Technol. 38 (5) (Mar. 2023) 055003, https://doi.org/10.1088/1361-6641/ACC2DF.
[46] Y. Kim, M. Kim, J.H. Hwang, T.W. Kim, S.S. Lee, W. Jeon, Sustainable resistance switching performance from composite-type ReRAM device based on carbon Nanotube@Titania core–shell wires, Sci. Rep. 10 (1) (Dec. 2020) 1–8, https://doi.org/10.1038/S41598-020-75944-3;SUBJMETA=301,638,639,925;KWRD=CHEMISTRY,MATERIALS+SCIENCE,NANOSCIENCE+AND+TECHNOLOGY.
[47] N. Mullani, et al., Improved resistive switching behavior of multiwalled carbon nanotube/TiO2 nanorods composite film by increased oxygen vacancy reservoir, Mater. Sci. Semicond. Process. 108 (Mar. 2020) 104907, https://doi.org/10.1016/J.MSSP.2019.104907.
[48] M. Commodo, et al., Resistive switching phenomenon observed in self-assembled films of flame-formed carbon-tio2 nanoparticles, Materials 14 (16) (Aug. 2021), https://doi.org/10.3390/MA14164672.
[49] C.S. McEnally, Ü.Ö. Köylü, L.D. Pfefferle, D.E. Rosner, Soot volume fraction and temperature measurements in laminar nonpremixed flames using thermocouples, Combust. Flame 109 (4) (Jun. 1997) 701–720, https://doi.org/10.1016/S0010-2180(97)00054-0.
[50] M. Ratova, G.T. West, P.J. Kelly, Optimization studies of photocatalytic tungsten-doped titania coatings deposited by reactive Magnetron Co-Sputtering, Coatings 3 (4) (Oct. 2013) 194–207, https://doi.org/10.3390/COATINGS3040194, 2013, *Vol.* 3, *Pages* 194-207.
[51] S.A. Zikalala, et al., Microwave-assisted synthesis of titania–amorphous carbon nanotubes/amorphous nitrogen-doped carbon nanotubes nanohybrids for photocatalytic degradation of textile wastewater, RSC Adv. 11 (12) (Feb. 2021) 6748–6763, https://doi.org/10.1039/D0RA08191D.
[52] H. Zhang, J.F. Banfield, Understanding polymorphic phase transformation behavior during growth of nanocrystalline aggregates: insights from TiO2, J. Phys. Chem. B 104 (15) (Apr. 2000) 3481–3487, https://doi.org/10.1021/JP000499J/ASSET/IMAGES/LARGE/JP000499JF00006.JPEG.
[53] S.Y. Lee, S.J. Park, TiO2 photocatalyst for water treatment applications, J. Ind. Eng. Chem. 19 (6) (Nov. 2013) 1761–1769, https://doi.org/10.1016/J.JIEC.2013.07.012.
[54] X. Xia, et al., Control of interface between anatase TiO2 nanoparticles and rutile TiO2 nanorods for efficient photocatalytic H2 generation, J. Power Sources 376 (Feb. 2018) 11–17, https://doi.org/10.1016/J.JPOWSOUR.2017.11.067.
[55] X. Chen, S.S. Mao, Titanium dioxide nanomaterials: synthesis, properties, modifications and applications, Chem. Rev. 107 (7) (Jul. 2007) 2891–2959, https://doi.org/10.1021/CR0500535/ASSET/IMAGES/LARGE/CR0500535F00044.JPEG.
[56] G. Liu, L. Wang, H.G. Yang, H.M. Cheng, G.Q. Lu, Titania-based photocatalysts—crystal growth, doping and heterostructuring, J. Mater. Chem. 20 (5) (Jan. 2010) 831–843, https://doi.org/10.1039/B909930A.
[57] R. Waser, M. Aono, Nanoionics-based resistive switching memories, Nat. Mater. 6 (11) (Nov. 2007) 833–840, https://doi.org/10.1038/nmat2023, 2007 6:11.
[58] M.Y. Manuputty, et al., Polymorphism of Nanocrystalline Tio 2 Prepared in a Stagnation Flame: Formation of the Tio 2-II Phase †, 2019, https://doi.org/10.1039/c8sc02969e.
[59] S.K. Kuriechen, S. Murugesan, S.P. Raj, Mineralization of Azo Dye using combined photo-fenton and photocatalytic processes under visible light, Journal of Catalysts 2013 (1) (Jan. 2013) 104019, https://doi.org/10.1155/2013/104019.
[60] H. Tang, F. Lévy, H. Berger, P.E. Schmid, Urbach tail of anatase, Phys. Rev. B 52 (11) (Sep. 1995) 7771, https://doi.org/10.1103/PhysRevB.52.7771.
[61] C. Di Valentin, G. Pacchioni, A. Selloni, Theory of carbon doping of titanium dioxide, Chem. Mater. 17 (26) (Dec. 2005) 6656–6665, https://doi.org/10.1021/CM051921H/ASSET/IMAGES/LARGE/CM051921HF00008.JPEG.
[62] P. Minutolo, G. Gambi, A. D'Alessio, The optical band gap model in the interpretation of the UV-visible absorption spectra of rich premixed flames, Symposium (International) on Combustion 26 (1) (Jan. 1996) 951–957, https://doi.org/10.1016/S0082-0784(96)80307-9.
[63] J.H. Miller, J.D. Herdman, C.D.O. Green, E.M. Webster, Experimental and computational determinations of optical band gaps for PAH and soot in a N2-diluted, ethylene/air non-premixed flame, Proc. Combust. Inst. 34 (2) (Jan. 2013) 3669–3675, https://doi.org/10.1016/J.PROCI.2012.05.054.
[64] S.H. Mohamed, M. El-Hagary, S. Althoyaib, Growth of undoped and Fe doped TiO2 nanostructures and their optical and photocatalytic properties, Appl. Phys. A Mater. Sci. Process. 111 (4) (Jun. 2013) 1207–1212, https://doi.org/10.1007/S00339-012-7367-7/FIGURES/7.

[65] K.C. Smyth, C.R. Shaddix, The elusive history of m~= 1.57 – 0.56i for the refractive index of soot, Combust. Flame 107 (3) (Nov. 1996) 314–320, https://doi.org/10.1016/S0010-2180(96)00170-8.
[66] S. Roy, S.P. Ghosh, D. Pradhan, P.K. Sahu, J.P. Kar, Investigation of morphological and electrical properties of RTA-processed TiO2 for memristor application, J. Sol. Gel Sci. Technol. 96 (3) (Dec. 2020) 702–717, https://doi.org/10.1007/S10971-020-05395-9/METRICS.
[67] N.A. Ahir, et al., Capacitive coupled non-zero I–V and type-II memristive properties of the NiFe2O4–TiO2 nanocomposite, Mater. Sci. Semicond. Process. 125 (Apr. 2021) 105646, https://doi.org/10.1016/J.MSSP.2020.105646.
[68] S.P. Adhikari, M.P. Sah, H. Kim, L.O. Chua, Three fingerprints of memristor, IEEE Transactions on Circuits and Systems I: Regular Papers 60 (11) (2013) 3008–3021, https://doi.org/10.1109/TCSI.2013.2256171.
[69] M. Lanza, et al., Recommended methods to Study resistive switching devices, Adv Electron Mater 5 (1) (Jan. 2019) 1800143, https://doi.org/10.1002/AELM.201800143;WGROUP:STRING:PUBLICATION.
[70] L.O. Chua, S.M. Kang, Memristive devices and systems, Proc. IEEE 64 (2) (1976) 209–223, https://doi.org/10.1109/PROC.1976.10092.
[71] D. Biolek, Z. Biolek, V. Biolkova, Pinched hysteretic loops of ideal memristors, memcapacitors and meminductors must be 'self-crossing, Electron. Lett. 47 (25) (Dec. 2011) 1385–1387, https://doi.org/10.1049/EL.2011.2913.
[72] G.A. Illarionov, S.M. Morozova, V.V. Chrishtop, M.A. Einarsrud, M.I. Morozov, Memristive TiO2: Synthesis, technologies, and applications, Front. Chem. 8 (Oct. 2020) 556815, https://doi.org/10.3389/FCHEM.2020.00724/BIBTEX.
[73] B. Sun, M. Xiao, G. Zhou, Z. Ren, Y.N. Zhou, Y.A. Wu, Non–zero-crossing current-voltage hysteresis behavior in memristive system, Mater. Today Adv. 6 (Jun. 2020) 100056, https://doi.org/10.1016/J.MTADV.2020.100056.
[74] J.S. Lee, S. Lee, T.W. Noh, Resistive switching phenomena: a review of statistical physics approaches, Appl. Phys. Rev. 2 (3) (Sep. 2015), https://doi.org/10.1063/1.4929512/13398693/031303_1_ACCEPTED_MANUSCRIPT.PDF.
[75] A.K. Jena, et al., Bipolar resistive switching in TiO2 artificial synapse mimicking Pavlov's associative learning, ACS Appl. Mater. Interfaces 15 (2) (Jan. 2023) 3574–3585, https://doi.org/10.1021/ACSAMI.2C17228/ASSET/IMAGES/LARGE/AM2C17228_0008.JPEG.
[76] I. Salaoru, Q. Li, A. Khiat, T. Prodromakis, Coexistence of memory resistance and memory capacitance in TiO2 solid-state devices, Nanoscale Res. Lett. 9 (1) (Oct. 2014) 1–7, https://doi.org/10.1186/1556-276X-9-552/FIGURES/5.
[77] S. Mao, et al., Mechanism and application of capacitive-coupled memristive behavior based on a biomaterial developed memristive device, ACS Appl. Electron. Mater. 3 (12) (Dec. 2021) 5537–5547, https://doi.org/10.1021/ACSAELM.1C00951/ASSET/IMAGES/LARGE/EL1C00951_0010.JPEG.
[78] J. Zhang, D. Chen, S. Huang, The role of oxygen vacancies in resistive switching behavior of organic-TiO2 hybrid composite, Appl. Phys. A Mater. Sci. Process. 123 (10) (Oct. 2017) 1–6, https://doi.org/10.1007/S00339-017-1219-4/FIGURES/6.
[79] S. Sharma, et al., Light-enhanced negative differential resistance and multi-level resistive switching in glutamine-functionalized MoS2 quantum dots for resistive random-access memory devices, Adv. Mater. Interfac. 10 (2) (Jan. 2023) 2201537, https://doi.org/10.1002/ADMI.202201537.
[80] F. Huang, et al., Light-induced multilevel resistive switching in cesium-doped lead-free halide double perovskite memory device, J. Alloys Compd. 1004 (Nov. 2024) 175827, https://doi.org/10.1016/J.JALLCOM.2024.175827.
[81] T. Paul, P.K. Sarkar, S. Maiti, K.K. Chattopadhyay, Multilevel programming and light-assisted resistive switching in a halide-tunable all-inorganic perovskite cube for flexible memory devices, ACS Appl. Electron. Mater. 2 (11) (Nov. 2020) 3667–3677, https://doi.org/10.1021/ACSAELM.0C00719/ASSET/IMAGES/LARGE/EL0C00719_0010.JPEG.